PCCP

Accepted Manuscript

ROYAL SOCIETY OF CHEMISTRY

www.rsc.org/pccp

Journal Name

RSCPublishing

ARTICLE

Silver nanoparticles linked by Pt-containing organometallic dithiol bridge: study on local structure and interface by XAFS and SR-XPS.

Cite this: DOI: 10.1039/x0xx00000x

Received 00th January 2012,
Accepted 00th January 2012

DOI: 10.1039/x0xx00000x

www.rsc.org/

C. Battocchio*[a], I. Fratoddi[b], L. Fontana[b], E. Bodo[b], F. Porcaro[a], C. Meneghini[a], I. Pis[c,d], S. Nappini[c], S. Mobilio[a], M.V. Russo[b], G. Polzonetti[a]

Silver nanoparticles (AgNPs) functionalized with an organometallic bifunctional thiol containing Pt(II) centers, generated in situ from *trans-trans*-[thioacethyl-bistributylphosphine-diethynylbiphenyl-diplatinum(II)] were synthetized with different sulphur/metal molar ratios (i.e. AgNPs-1 and AgNPs-2) with the aim to obtain nanosystems of different mean size and self-organization. AgNPs spontaneously self-assemble, giving rise to 2D networks, as previously assessed. In this work a deeper insight into the chemico-physical properties of these AgNPs is proposed by means of synchrotron radiation induced X-ray Photoelectron Spectroscopy (SR-XPS) and X-ray Absorption Fine Structure spectroscopy (XAFS) techniques. The results are discussed in order to probe the interaction at the interface between noble metal and thiol ligand at atomic level and the aim of this study is to shed light on the nanosystems chemical structure and self-organization details. The nature of the chemical interaction between the dithiol ligand and the Ag atoms on the nanoparticle surface was investigated combining SR-XPS (S2p, Ag3d core levels) and XAS (S and Ag K-edges) analysis. UV-visible absorption and emission measurements were also carried out on all samples and compared with TD-DFT calculations as to get a better understanding of their optical behavior and establish the nature of the excitation and emission processes.

Introduction

In recent years, noble metal nanoparticles functionalized with molecular ligands emerged as potential materials for applications in different areas ranging from electronics to optics, catalysis, sensors and biotechnology.[1] As a consequence, considerable effort has been devoted to the synthesis and characterization of these materials. Among other noble metal nanoparticles (MNPs), silver nanoparticles (AgNPs) show peculiar optical and magnetic behavior as the dimension approaches the Fermi wavelength of electrons in subnanometer regime; for example, they are found to exhibit strong size-dependent fluorescent emission [2] and ferromagnetic behavior [3,4].

The characteristic plasmonic properties of MNPs are strongly dependent on inter-particles interactions, since in the near-field adjacent particles may couple together the plasmon oscillations. The frequency of coupled-particle Localized Surface Plasmon Resonance (LSPR) is generally shifted from the single particle resonance depending on the strength of the inter-particle coupling that, in turn, is a function of inter-particle spacing. Therefore, obtain conveniently spaced nanoparticles with sharp interparticle distance distribution is mandatory for applicative purposes [5].

Bi-functional ligands with intrinsic self assembling properties are specially suited in this context [6], as they produce ordered 2D or 3D networks with reproducible interparticle spacing. Recently, some of us demonstrated that organic and organometallic dithiols can be successfully used to stabilize gold or silver nanoparticles, leading to complex arrangements in dyads [7, 8, 9]. It should be noted that the LSPR is definitively affected by the nature of MNPs surface (*i.e.* sharp interfaces or core-shell morphology) and by the chemical bonds at the interface between the capping agents and the metal. Such

understanding requires complementary state of the art investigation techniques, such as Synchrotron Radiation induced X-ray Photoelectron Spectroscopy (SR-XPS) and X-ray Absorption Fine Structure (XAFS) spectroscopy. In fact, SR-XPS is extensively used to investigate the sulfur-metal bond of self-assembled monolayers of organometallic thiols on flat surfaces [10,7] as well as MNPs [11,12]. In particular, the high surface to volume ratio of metal nanoparticles makes them ideally suited to SR-XPS measurements. Moreover, XAFS investigations at Ag and S K-edges allow an accurate assessment of local atomic structure parameters [13]. Combining complementary information from XAFS and SR-XPS offers the valuable possibility to deeply understand particle size and morphology as recently demonstrated with small thiols capped Ag nanoparticles [14].

Hereafter, a detailed SR-XPS and XAFS study of silver colloids capped with organometallic Pt-based dithiols, in situ generated from the complex *trans*- *trans*-[CH_3CO-S-$Pt(PBu_3)_2(C{\equiv}C$-C_6H_4-C_6H_4-$C{\equiv}C)$-$Pt(PBu_3)_2$-S-$COCH_3$] (**complex (1)**) to give the -SH derivative covalently bound to Ag, is reported The chemical interaction arising between the Ag metal atoms at NPs surface and bifunctional organometallic ligand has been investigated. The choice of this complex is due to the optical and sensing properties of Pt ethynylated complexes and polymers [15, 16, 17] that could be coupled with the optical and biochemical features of Ag nanostructures [18]; furthermore, previous studies on homologue organometallic ligands on gold nanoparticles showed interesting optical properties [11, 19].

Previous investigation [8] carried out combining high resolution electron-transmission microscopy (HR-TEM), selected area electron diffraction (SAED) and energy-dispersive X-ray diffraction (EDXD) on a 1/1 silver/tiol molar ratio material, have pointed out the AgNPs self-organization in 2D networks. In this work, our aim is to probe the local atomic (XAFS) and electronic (SR-XPS) structure of AgNPs in particular focusing on the nature of the thiol/AgNP interface, in order to understand the relationship between self-assembling features and the chemical composition, structure and morphology. Two different silver/thiol molar ratios were used to prepare differently functionalized nanoparticles, *i.e.* 0.7/1 and 1/1, obtaining AgNPs-1 and AgNPs-2, respectively.

Furthermore, as to probe the unique optical properties of these materials, an UV-visible absorption and emission study was carried out. It was observed, that by varying the excitation wavelength in luminescence measurements, it is possible to finely tune both emission maxima wavelengths and intensities. Theoretical calculations were performed on two realistic molecular models and allowed us to fully describe and interpret the absorption and emission spectral features.

For many applications, the tunability of the optical properties is of paramount importance, which is dictated among others, by the size, shape, and assembly of nanoparticles. [9] Albeit the optical features are mainly core-derived, surface linkers play also an important role in shaping the electronic properties of the functionalized nanoparticles. In this context, plasmonic applications of Ag nanoparticles are of main interest ranging from the detection of molecules to surface enhanced fluorescence [20,21]. Recent studies have demonstrated the possibility of address the optical properties of 2D or 3D assembled metal nanoparticles [22], giving rise for example to coherent plasmonic effects [23,24], among others spacers [25].

Results and discussion

The silver nanoparticles stabilized with the organometallic bis-thiol, *in situ* obtained from **complex (1)**, were prepared with Ag/S molar ratio 0.7/1 and 1/1, by using a modified Brust's two-phase procedure [26,27,28] consisting in a chemical reduction of $AgNO_3$ in the presence the thiol ligand, $NaBH_4$ as reducing agent and tetraoctylammonium bromide (TOAB) as phase transfer agent. The thioacetyl deprotection occurs and the bifunctional thiol is generated during the synthesis. [29]

XAS data analysis results

The quantitative XAFS data analysis has been carried out along the lines previously described [14]. The Ag K-edge extended x-ray absorption fine structure (EXAFS) signals are reported in the following **Figure 1**, together with the chemical structure of AgNPs functionalized with the organometallic dithiol *trans*-*trans*-[H-S-$Pt(PBu_3)_2(C{\equiv}C$-C_6H_4-C_6H_4-$C{\equiv}C)$-$Pt(PBu_3)_2$-S-H].

It can be observed that the main contribution to the structural Ag K edge EXAFS signal arises from silver ions in the metallic fcc phase (Ag_M); as shown in the figure, an additional contribution, that can be assigned to an Ag-S phase, is required by the analysis. In AgNPs-1 such a contribution is limited to the first Ag-S shell, around 2.42 Å. On the contrary this contribution appears more intense and more ordered at medium range in AgNPs-2: here two next neighbor Ag-Ag shells must be included around 3.2 Å and 3.6 Å. This finding suggests thicker shell phase in AgNPs-2. Noticeably these additional Ag-Ag next neighbor distances are different from those of Ag_2S phase documented on [14] this suggest the Ag-S shell phase different from Ag_2S: Ag-Ag distances around 3.2 Å are found by High resolution TEM studying Ag rich metastable Ag_8S structure [30] formed during the early stages of Silver sulfidation.

a)

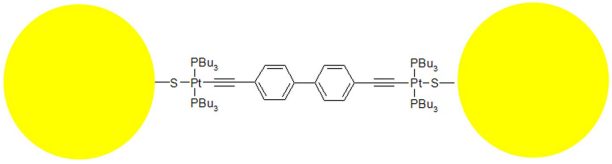

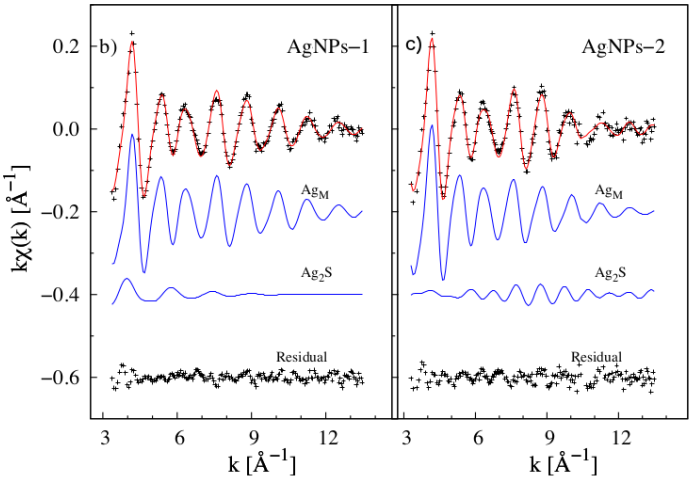

Figure 1. a) Chemical structure of AgNPs functionalized with the organometallic dithiol *trans- trans*-[H-S-Pt(PBu_3)$_2$(C≡C-C_6H_4-C_6H_4-C≡C)-Pt(PBu_3)$_2$-S-H]; in b), c) Ag K edge kχ(k) experimental (dots) and best fit (full line, red online) are presented for AgNPs-1 and AgNPs-2 samples. The partial contributions used in the analysis are shown for completeness, vertically shifted for clarity. The Ag_M terms include single and multiple scattering contributions from Ag fcc metallic phase (see text). The residuals: k (χ^{exp}-χ^{th}) are also shown at the bottom. Comparing the data in the two panels the AgNPs-2 sample presents larger Ag_M and weaker Ag-S contribution intuitively suggesting larger particles in AgNPs-2 than AgNPs-1.

In order to reduce the number of free parameters in the fitting, physical constraints were applied: the structural Ag_M phase is modeled using 4 contributions representing the first 4 Ag-Ag coordination shells of fcc structure [14]: R_I being the Ag-Ag bong length, $R_{II} = R_I(2)^{1/2}$, $R_{III} = R_I(3)^{1/2}$, $R_{IV} = 2R_I$. The coordination number of the i-th shell is calculated as $xN_i^{bulk}(1-pR_i)$, N_i^{bulk} being the bulk coordination number (N_1^{bulk}=12, N_2^{bulk}=6, N_3^{bulk}=24, N_4^{bulk}=12), x the fraction of Ag atoms in the fcc phase, the $(1-pR_i)$ term takes into account for the coordination number reduction due to the finite size of NPs [14,31], assuming roughly spherical particles $p\sim0.75/R_{NP}$ [31]. R_I, x, and R_{NP} were refined together with σ^2_i. An additional contribution has been added to take into account for Ag-S phase, assuming (1-x) fraction of Ag in Ag_2S-like phase. Two shells are used for the AgNPS-1 sample: Ag-S at R_{AgS} ~ 2.5 Å with multiplicity number N_{AgS}^{bulk} ~ 2 and Ag-Ag at R_{AgAg} ~ 3.2 Å with multiplicity number N_{AgAg}^{bulk} ~ 5. Noticeable the contributions from this Ag_2S-like phase appear more intense and more structured in the Ag-NPS-2 sample suggesting a thicker and more ordered phase. In this sample two next neighbor Ag-Ag shells must be considered in the analysis at about 3.2 Å and 3.6 Å (see supporting information).

Table 1. Main structural parameters obtained by Ag K-edge XAFS data analysis: x is the fraction of Ag ions into the metallic phase, the parameter p is used to calculate the Ag_{NP} diameter D_{NP}=1.5 / p (see text), R_I is the Ag-Ag nearest neighbour bond lenght, the next neighbour distances are contrained to R_I by the fcc geometry, R_{Ag-S} the Ag-S interatomic distance.

sample	x	p(x10^2)	R_I	D_{NP}	R_{Ag-S}
		[Å^{-1}]	[Å]	[Å]	[Å]
AgNPs-1	0.77(5)	6.2(15)	2.846(8)	24(6)	2.42(2)
AgNPs-2	0.72(5)	3.5(8)	2.858(9)	43(10)	2.38(3)

Quantitative analysis suggests the AgNPs-1 sample have smaller Ag_M NPs with diameter D~2.4 nm, while AgNP-2 have D~4.5 nm. The Ag-Ag and Ag-S distances are closely similar (see Table 1) within the errors. In both samples the fraction of Ag into the Ag_M phase is around 75%. The Ag-S distance appears slightly shorter on AgNPs-2 sample.

The quantitative analysis of S-K edge provides more details about Ag-thiol interface structure [14].
In these samples the Pt-M_3 edge is expected to occur around 2645 eV and must be taken into account during the extraction of S-K edge EXAFS data because a fraction of Pt-M_3 fluorescence goes into the resolution windows of fluorescence detector. In the ESTRA program [32] the contribution of Pt-M_3 edge has been included as arc-tangent function centered at 2647 eV added to the bare atomic background. The ratio between the edge discontinuity of Sulfur (J_S) and Pt (J_{Pt}) is weak, being around J_{Pt}/J_S =0.035 (AgNP-2) and J_{Pt}/J_S =0.039 (AgNP-1) therefore the Pt-M_3 fine structure oscillations can be safely neglected in the S EXAFS data analysis.
The analysis of the S-K edge EXAFS data has been carried out mainly considering the S atoms bridging the organometallic thiols to the Ag nanoparticles. Accordingly to [33] the structure of S-tail of the organometallic thiols is presented in Scheme 1: R_{S-Pt} =2.3 Å, R_{Pt-P} = 2.3 Å and R_{Pt-C} = 2.0 Å.

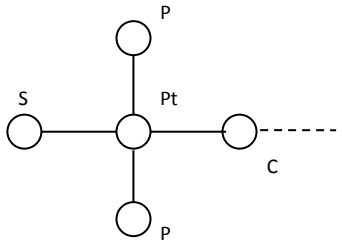

Scheme 1. Structure of S-tail of the organometallic thiol.

In the analysis, the following contributions were used: S-Pt, S-P and S-(Pt)-C, the last includes single and multiple scattering terms which are enhanced by the collinear S-Pt-C configuration (focusing effect). The coordination numbers were constrained to yN_i^{Thiol}, N_i^{Thiol} being the coordination numbers of S in pure

organometallic thiol: $N_{S\text{-}Pt}^{Thiol}$=1, $N_{S\text{-}P}^{Thiol}$=2, $N_{S\text{-}C}^{Thiol}$=1. Finally a S-Ag shell is included to take into account for thiol-NP binding. Since we are unable to distinguish S in a Ag_2S phase from S bridging Ag to Pt at the NP surface, therefore a single contribution is used: the S-Ag coordination number has been constrained assuming 4 Ag neighbors for S in Ag_2S phase and a single Ag bonded to bridging Sulfur, i.e. $N_{S\text{-}Ag}$= y + 4(1-y), 1-y being the fraction of S in the Ag_2S shell phase.

Table 2. the main structural parameters obtained by S K-edge XAFS data analysis: y is the fraction of S ions into the Ag_2S phase.

sample	y	$R_{S\text{-}Ag}$	$R_{S\text{-}Pt}$	$R_{S\text{-}P}$	$R_{S\text{-}Pt\text{-}C}$
		[Å^{-1}]	[Å]	[Å]	[Å]
AgNPs-1	0.61(4)	2.46(3)	2.31(2)	3.20(2)	4.25(3)
AgNPs-2	0.51(3)	2.48(2)	2.33(2)	3.20(2)	4.38(5)

The S-Pt, S-P and S-C distances are consistent with the S-thiol structure with minor differences between the two samples, indicating that the molecular structure of the organometallic dithiol is preserved during AgNPs grafting for most molecules, i.e. the organometallic moiety is chemically stable. The main difference is found at the S-Ag shell: here the fraction of S in the Ag_2S phase (1-y) is larger in AgNPs-2 suggesting that larger nanoparticles present thicker interface shell.

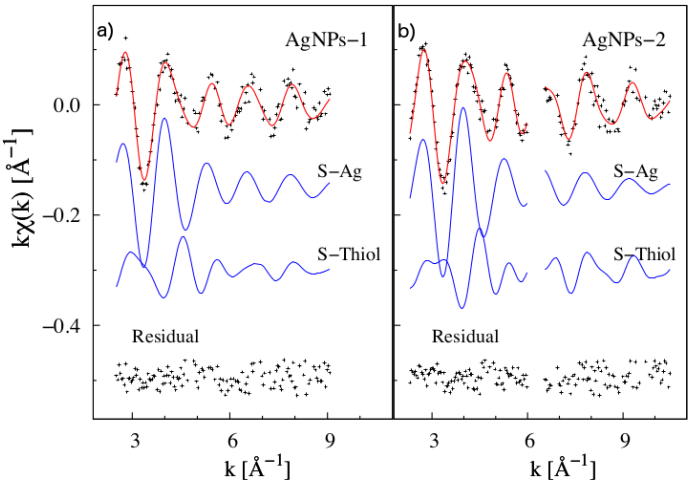

Figure 2. S-K edge data analysis on AgNPs-1 and AgNPs-2 samples. Experimental (dots) and best fit (full line, red online) kχ(k) are shown. The partial contributions are shown vertically shifted for clarity: the S-Thiol curves group together the S-Pt, S-P and S-C single scattering contributions, and the S-Pt-C multiple scattering terms. At the bottom the residual $k(\chi^{exp} - \chi^{th})$ are presented for completeness.

Synchrotron Radiation-induced X-ray Photoelectron Spectroscopy results

AgNPs-1 and AgNPs-2 samples were characterized by means of Synchrotron Radiation-induced X-ray Photoelectron Spectroscopy (SR-XPS), with the aim of investigating the chemical interaction arising between the silver NPs and the thiol obtained from **complex (1)**. C1s, Pt4f, P2p, S2p and Ag3d signals were collected and analysed; the measured Binding Energies (BE), full width half-maxima (FWHM) and atomic ratios were similar for the two analysed samples (for complete BE, FWHM and atomic ratio values see **Table S3** in the supporting information).

The main C1s peak is located at 285.00 eV, corresponding to aliphatic C atoms; two more components were individuated at higher BE values by following a peak fitting procedure: the component at 286.76 eV is attributed to C atoms bonded to S; the very small contribution at about 288.6 eV (nearly 1% of the entire C1s signal) is associated to carboxylate ions, probably arising by contamination species on the sample surface. P2p and Pt4f BEs are respectively $Pt4f_{7/2}$ BE = 73.00 eV, $P2p_{3/2}$ B.E. = 130.31 eV, as expected for binuclear compounds of Pt-poly-ynes PtDEBPn [34], evidencing that the organometallic molecules are all surface-associated and that Pt-S bond cleavage is not occurring [7]. A small component at lower BE values is also observed in Pt4f spectra (reported in **Figure 3**), and attributed to Pt atoms electronically interacting with the ethynyl-biphenyl groups of adjacent molecules, as expected for rod-like poly-ynes giving rise to metal-to-ligand (MLCT) intra and inter-molecular charge transfer [35].

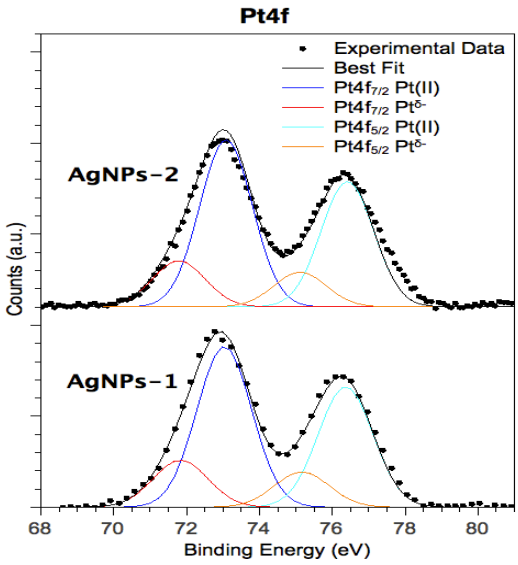

Figure 3. XPS Pt4f spectra collected on AgNPs-1 (bottom) and AgNPs-2 (top); spin-orbit components associated to Pt(II) atoms are in blue ($4f_{7/2}$ component) and cyan ($4f_{5/2}$); the signal attributed to Pt atoms acting as electron-acceptors from etynyl-biphenyl electron-rich moieties of adjacent molecules is in red ($Pt4f_{7/2}$) and orange ($Pt4f_{5/2}$).

In fact, **complex (1)** molecules are well known to give rise to self-assembling structures, due to the highly favorable interchain interactions arising between metal centers and adjacent acetylene moieties and aromatic rings; some of us already observed and reported this behavior in a study about the

self-assembling organization of dinuclear Pd(II)-based complexes anchored on gold surfaces [36] and of organometallic polymetallayynes [37].

As also indicated by the S K-edge and Ag K-edge XAFS analysis results, the most indicative signals for the individuation of the local structure at AgNPs/thiols interface are S2p and Ag3d core levels. These spectra are reported in **Figure 4a** and **b** (AgNPs-1 at the bottom, AgNPs-2 in the top).

S2p spectra are reported in **Figure 4a**; for both samples a large signal with a pronounced asymmetry is observed, suggesting that sulfur atoms are in at least two different chemical states. The peak fitting procedure allows for individuating two pair of spin-orbit doublets: the spin-orbit pair at lower BEs, $S2p_{3/2}$ BE = 160.75 eV, is due to organometallic thiols chemically linked to metals through a covalent S-metal bond [7,10]. The signal at higher BE (about 163 eV) is associated to sulfur atoms of free thiol terminal groups, as already observed for organometallic thiols deposited onto metal surfaces [10]. It is noteworthy that the S2p spectrum shows no evidence of oxidized sulfur, which normally appears at 167 eV [38]. From a semiquantitative point of view, the S-Ag atomic percent is 77.3% for AgNPs-1 and 75% for AgNPs-2, while the remaining 22.7% (AgNPs-1) and 25% (AgNPs-2) is of free thiol terminal groups. This finding suggests that about 75% of dithiol molecules bond silver atoms with both terminal groups, in a bridge-like configuration. In fact, rod-like **complex (1)** molecules appear too rigid to organize themselves in a clip-like structure which should lead to link both terminal groups to the same NP. Furthermore, HR-TEM images reported in [8] suggested the formation of AgNP-dithiols-AgNP dyads, as well as the presence of free **complex (1)** molecules and dithiols grafting nanoparticles surface with only one end-group.

In **Figure 4b**, Ag3d SR-XPS spectra are reported. The measured spectra appear asymmetric, and by applying a peak fitting procedure two spin-orbit pairs have been individuated. The main spin-orbit pair is found at BE values expected for metallic silver signal ($Ag3d_{7/2}$ BE = 368.24 eV). The less intense couple of components at higher BE ($Ag3d_{7/2}$ BE = 368.96 eV) are attributed to positively charged Ag atoms belonging to the NPs surface and chemically interacting with sulfur, coherently with Ag K-edge XAS results and literature data [14]. Similar results are observed at sulfur and silver core levels for both AgNPs-1 and AgNPs-2, indicating that the two samples have analogous electronic and chemical structures and different mean size.

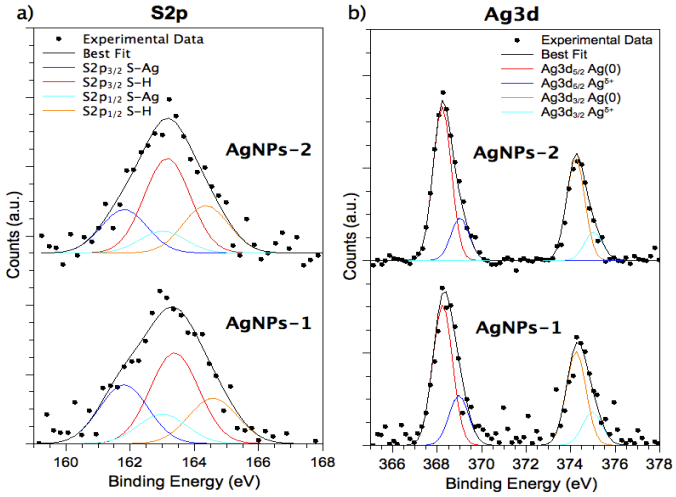

Figure 4. a) S2p spectra collected on AgNPs-1 (bottom) and AgNPs-2 (top); both spectra show a less intense couple of spin-orbit components at lower BE values (blue-cyan), due to S atoms covalently bonded to Ag atoms on NPs surface, and a more intense spin-orbit pair at higher BE values (red-orange), due to free thiol terminal groups of unbonded or physisorbed molecules. b) Ag3d spectra of AgNPs-1 (bottom) and AgNPs-2 (top); the main spin-orbit pair (red-orange) is due to metallic silver atoms, the small couple of components at higher BE values (blue-cyan) are indicative for Ag atoms covalently bonded to the S atoms of thiol end groups.

UV-visible Absorpion and Emission measurements data analysis

The coupling between the peculiar emission behavior of Pt(II) dithiols and the optical features of Ag nanostructures, combined with the organization in 2D networks, are expected to influence and modulate the optical properties of the studied AgNPs, dramatically differencing them from those shown by the pristine **complex (1)** [39, 40]. With the aim to probe the unique optical properties of these materials, an extensive UV-visible absorption and emission study was carried out on both AgNPs-1 and AgNPs-2.

The characterization of AgNPs-1 and AgNPs-2 highlighted the presence of a π- π* band centered at 350 nm, arising from the organometallic ligand [41], and a shoulder at about 410 nm that supported the formation of silver nanoparticles [42].

Emission measurements were carried out using different excitation wavelengths, as to enhance in turn the luminescence yield from the organometallic moiety or AgNP. Both emission wavelengths and intensities were affected by the excitation wavelength choice. As reported in **Figure 5a** and **b**, both samples showed different emission maxima that were enhanced by different excitations. In **Figure 5c** and **d**, the same trend is reported in 3D correlating excitation, emission wavelengths and emission intensities. It is noteworthy that the two nanosystems show emission intensity maxima at different wavelengths of excitation and emission (AgNPs-1: λecc.max. = 290 nm λem.max. = 350 nm; λexc.max. = 340 nm, λem.max. = 430 nm; AgNPs-2: λexc.max. = 290 nm λem.max. = 380 nm;

λexc.max. = 370 nm, λem.max. = 460 nm); these wavelength values are influenced by NPs mean size, as predicted by literature [39].

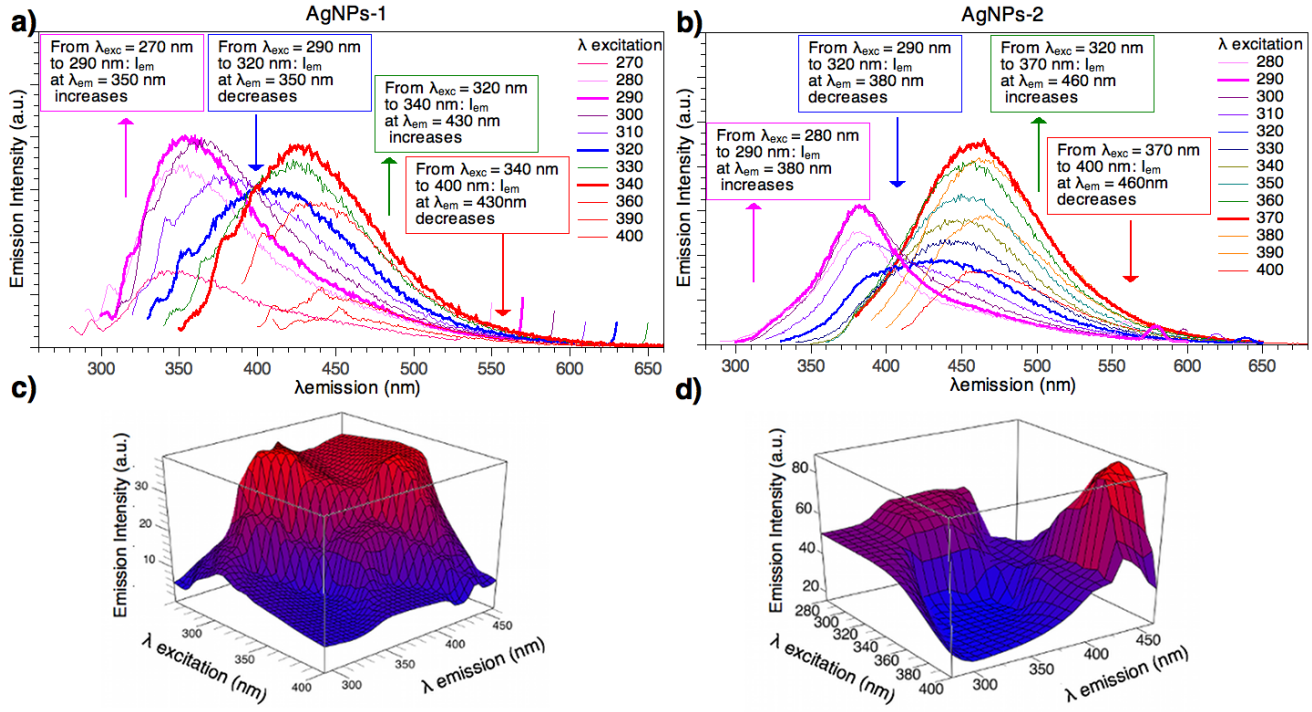

Figure 5. a), b) UV-visible emission spectra obtained with different excitation wavelength for respectively AgNPs-1 and AgNPs-2; c), d) emission spectra of samples AgNPs-1 and AgNPs-2 reported in 3D correlating excitation, emission wavelengths and emission intensities.

Calculations

Calculations have been performed on two model systems in the gas phase. The models are composed by the organic linker -S-$(PH_3)_2$-C≡C-C_6H_4-C_6H_4-C≡C-Pt$(PH_3)_2$-S- connected either to one (Ag-link-H) or two Ag atoms (Ag-link-Ag). The optimized geometries are reported in **Figure 6**. In the compound Ag-link-H, an H atom has been added on the other terminal sulphur in order to provide a saturated molecule, though this atom is not visible in **Figure 6**. The computations have been performed using Gaussian09 [43]. We have used the B3LYP functional in conjunction with a 6-31G(d) basis on the light atoms and the LANL2DZ basis and ECP on the heavy metal. The TDDFT excitation calculations have followed a full geometric optimization. TDDDFT calculations provided the location of the first 40 excited states for both models including 20 triplet and singlet states. The TDDFT calculations have been perfrmed by simulating the solvent presence via PCM with default parameters for dichloromethane. The geometries that have been found are in good agreement with the XAS data reported above: the distances between the atoms are comparable and in particular we find that the distances $R_{Ag\text{-}S}$, $R_{S\text{-}Pt}$, $R_{S\text{-}P}$ and $R_{S\text{-}Pt\text{-}C}$ are 2.37, 2.44, 3.27 and 4.43 respectively. Give that we model the Ag presence by means of a single terminal atom it is natural that the $R_{Ag\text{-}S}$ and the $R_{S\text{-}Pt}$ differs the most from the experimental ones.

Table 3: Calculated absorption wevelengths and oscillator strengths for the two molecular models.

Model	State	nm	Excitations (dominant)	Osc. Strength
Ag-link-H HOMO=132	S1	490	131→133	0.01
	S2	425	130→133 **132→133**	0.29
	S4	377	130→136 **132→134** 132→136	1.4
	S6	370	mixed	0.25
	S14	313	mixed	0.1
Ag-link-Ag HOMO=141	S1	492	139→142 140→143	0.01
	S3	423	138→143 139→142 **141→142**	0.45
	S7	377	mixed	0.17
	S8	377	mixed	0.26
	S9	375	**141→144** 139→142 140→143	0.97
	S15	360	139→144	0.3

We present the result for the absorption process in Table 3 where we show the details of the transitions between the singlet states. We limit the presentation only to those states that have oscillator strengths larger than 0.1. As an exception we also report the lowest lying singlet states. A Lorentzian convolution over the "stick lines" provides the absorption spectra reported in **Figure 7**. The Ag-link-H and Ag-link-Ag compounds present two distinct absorption maxima around 425 and 375 respectively in agreement with the measured absorption maxima around 410 and 350 where, it must be noted, both the nature of the terminal metal and the aggregation state of the compounds are different from our models.

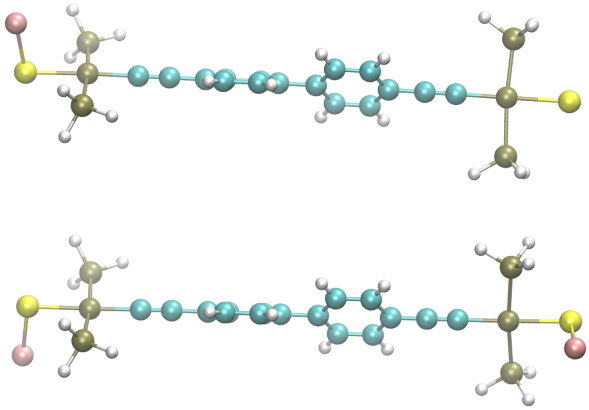

Figure 6. Model compounds for the gas-phase calculations. Geometry optimized at the b3lyp/6-31G(d)/LANL2DZ level.

The transitions are originated by a relative complex pattern of single particle excitations between the Kohn and Sham orbitals. The orbitals involved are reported in Figure S1 (Supporting Information).

The HOMO in both model systems is quite straightforwardly made by the two conjugated systems of the phenyl and of the acetylene units and shows no contribution from the metal (see Figure S1). The LUMO is instead substantially made only by a sigma anti-bonding orbital along the S-Ag bonds. While the former is delocalized over the entire molecule the latter remains rather localized. The first intense absorption band that lies at 425 nm is due to a HOMO→LUMO excitation process, which corresponds to excitation to state S2 and S3 for Ag-link-H and Ag-Link-Ag respectively. This transition "moves" the electron from the π orbital to the empty σ* orbital localized on the S-Ag bond. This result is in agreement with the common interpretation that this absorption is due to plasmon resonance. The intense absorption lines at 375 nm are, instead, due to a typical π-π* transition that involve (see Table 3) the LUMO+1 (Ag-link-H) or the LUMO+2 (Ag-link-Ag) orbitals on the organometallic linker. The transitions promoting the HOMO electrons into these orbitals are those responsible for the most intense absorption bands.

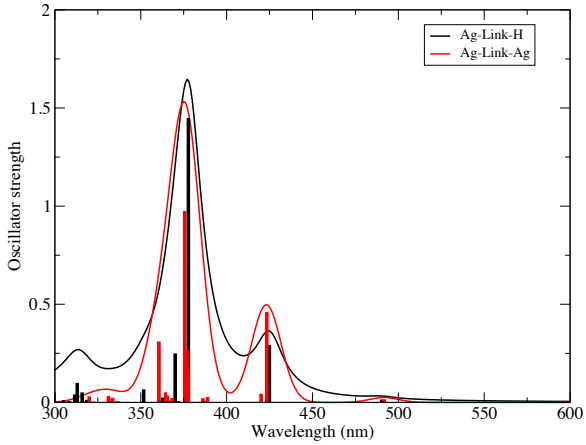

Figure 7. TDDFT predicted spectra: "stick" spectra are reported as bars, while the convoluted ones have been calculated by assuming a gaussian width of 50 nm.

Given the existence of a first strong absorbing excited state around 425 and the presence of several equally optically active states between 380 and 360 nm (see Figure 7), we can interpret the measured emission profile as the result of emission coming from these states. In the following we assume that the non radiative decay processes in these systems, despite the presence of the metal atoms, are so inefficient or at least so slow (less than a ns) to allow fluorescence to occur. The irradiation at low energies around 340 nm will primarily pump population into the first, optically active excited state (S2 for Ag-link-H or S3 for Ag-link-Ag). The excitation is then probably followed by an extremely rapid vibrational deactivation and then by the emission at slightly longer wavelengths. When we irradiate the system with higher photon energies up to 290 nm we populate the highest excited states (for example we find S4 for Ag-link-H and S9 for Ag-link-Ag). These states can then emit, after vibrational decay, around 350-370 nm. In Figure 8 we draw a cartoon of the absorption and emission processes using the calculated excitation energies of the Ag-link-H model. We show two typical scenarios depending upon the irradiation frequency (left for a high wavelength and right for a lower one). Assuming that internal conversion or intersystem crossing is inefficient, the double maxima structure noticed in the experimental emission profiles is simply the consequence of the exited state structure, density and spacing. In other words, when the irradiation energy is low we mainly excite the plasmonic absorption band at 425 nm. If our modelling is correct, we can conclude that the ensuing emission at higher wavelengths (430-500 nm in **Figure 5**) is arguably mainly coming from the Ag nanoparticle. Increasing the excitation energy moves the population to the higher excited states and produces the other emission band at lower wavelength that, in the experiments, can be seen around 350 nm. By using our molecular model as a guide, we can say that this latter emission is mainly due to the organometallic linker.

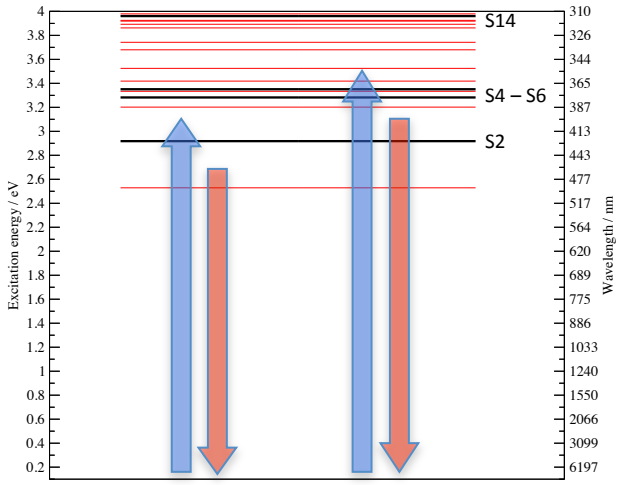

Figure 8. Excitation energy level scheme and approximate absorption (blue arrows) and emission (red arrows) wavelengths for compound Ag-link-H. The optically inactive singlet states are drawn in red those with oscillator strengths larger than 0.1 are plotted in black.

Experimental

Materials

Silver nitrate ($AgNO_3$, Aldrich, 99.5%), tetraoctylammonium bromide (TOAB) (Aldrich 98%), potassium tetrachloroplatinate (K_2PtCl_4, Aldrich, 99.9+%), tributylphosphine (PBu_3, Aldrich, 98%), potassium thioacetate (CH_3COSK, Aldrich, 98%), sodium borohydride ($NaBH_4$, Aldrich, 99%) and organic solvents (Aldrich reagent grade) were used as received.
Platinum complex *trans*-[dichlorobis(tributylphosphine)platinum(II)] and 4,4'-diethynylbiphenyl (H-C≡C-C6H4-C6H4─C≡C-H, DEBP) were prepared by reported methods [44,45]. Preparative thin-layer chromatography (TLC) separation was performed on 0.7 mm silica plates (Merck Kieselgel 60 GF254) and chromatographic separations were obtained with 70-230 mesh silica (Merck), by using n-hexane/dichloromethane mixtures. Deionized water (18.2 MΩ), obtained from Zeener Power I Scholar UV instrument was degassed for 30 minutes with Argon, before use. Other solvents and materials were reagent grade (Aldrich).
The synthesis and characterization of *trans, trans*-[CH_3CO-S-$Pt(PBu_3)_2$(C≡C-C_6H_4-C_6H_4-C≡C)-$Pt(PBu_3)_2$-S-$COCH_3$] (**complex (1)**) has been reported in a recent paper [7] with a ligand substitution reaction in the presence of potassium thioacetate in equimolar amount with *trans, trans*-[$ClPt(PBu_3)_2$-C≡C-C_6H_4-C_6H_4-C≡C-$Pt(PBu_3)_2Cl$] and its main characterizations are herein reported: IR (film, cm^{-1}): 2117 (C≡C), 1622 (C=O), 1600 (phenyl), 1260 (S-C=O). UV- vis (CH_2Cl_2): λ_{max} = 347 nm.

The AgNPs were prepared at room temperature in a two-phase system, modifying the Brust-Schriffin procedure [8,20] and using two different Ag/S molar ratios, i.e. 0.7:1 (AgNPs-1) and 1:1 (AgNPs-2). A toluene solution of **complex (1)** (230 mg, 1.48 x 10^{-4} mmol, toluene 10 mL) is mixed with $AgNO_3$ (51.0 mg, 2.97x10^{-4} mmol, H_2O 5 mL) in the 1:1 Ag/S molar ratio and dissolved in de-ionized water together with a toluene solution of TOAB, and then a $NaBH_4$ water solution is added. Then 86.5 mg (0.158 mmol) of TOAB in 10 mL of toluene were added and the solution turned yellow; after the further of 62.4 mg of $NaBH_4$ dissolved in 4 ml of de-ionized water, a brown color appeared into the reaction mixture that was allowed to react for 2 h at room temperature under magnetic stirring. At the end, extraction with H_2O followed and the obtained brown solid was isolated by evaporation of the organic layer. The solid was re-suspended in absolute ethanol, deposited by centrifugation and purified with water 5 times by centrifugation at 5000 rpm and recovered with a total yield 32%. FTIR characterization: (film, cm^{-1}): 2111 (C≡C), 1629 (C=O), 1602 (phenyl), 1487, 1462; UV- vis (CH_2Cl_2): λ_{max} = 348 nm, 415 nm.

Characterizations

SR-XPS experiments were carried out at ELETTRA storage ring using the experimental set-up of the BACH (Beamline for Advanced DiCHroism) beam-line. The BACH beamline exploits the intense radiation emitted from an undulator front-end. XPS measurements were performed in the fixed analyser transmission mode with the pass energy set to 30 eV. X-ray energies E_1=380 eV and E_2=500 eV have been used to probe the C1s, P2p, Pt4f, S2p and Ag3d spectral regions; the photon energy of each XPS spectrum was selected optimizing the photoelectron yield of the corresponding core level. The monochromator entrance and exit slits were fixed at 30 µm. The achieved resolving power was of 0.22 eV. Calibration of the energy scale was made referencing all the spectra to the gold Fermi edge of an Au reference sample. Curve-fitting analysis of the C1s, P2p, Pt4f, S2p, Ag3d spectra was performed using gaussian curves as fitting functions. $S2p_{3/2,1/2}$, $Ag3d_{5/2,3/2}$ and $Pt4f_{7/2,5/2}$ doublets were fitted by using the same full width at half-maximum (FWHM) for each pair of components of the same core level, a spin-orbit splitting of respectively 1.2 eV, 6.0 eV and 3.3 eV and branching ratios $S2p_{3/2}$ / $S2p_{1/2}$ = 2/1, $Ag3d_{5/2}$ / $Ag3d_{3/2}$ = 3/2 and $Pt4f_{7/2}$ / $Pt4f_{5/2}$ = 4/3. When several different species were individuated in a spectrum, the same FWHM value was used for all individual photoemission bands.

X-ray absorption spectra were collected at the S K-edge (E_S=2472 eV) and Ag K-edge (E_{Ag}=25514 eV). S K-edge XAS experiments were carried out at the 11.1-XAFS beamline at the ELETTRA synchrotron radiation storage ring (Trieste, Italy): the 11.1-XAFS beamline is equipped with two independent Si [111] crystals monochromator and harmonic rejection mirrors. The S K-edge XAFS signal has been measured at room temperature in fluoresce geometry using a single element Ketek solid-state detector whose energy resolution allows to

selectively collecting the S Kα fluorescence signal. The data were normalized by the incident intensity measured using a ionization chamber placed before the sample. Up to twenty spectra were measured for each sample and averaged up to achieve statistics suitable for reliable data analysis.

Ag K-edge XAFS experiments were carried out at the BM08-GILDA beamline at the European synchrotron radiation facility, ESRF (Grenoble, France)[46]. The beamline is equipped with two independent Si [311] crystals monochromator, working in sagittal focusing geometry and harmonic rejection mirrors. The Ag K-edge XAFS signal has been measured keeping the sample at the liquid nitrogen temperature, in fluorescence geometry using a 13-elements high purity Ge multidetector to selectively measure the Ag K_α fluorescence intensity. The data collected by each detector were summed up and normalized to the incident intensity measured using a ionization chamber placed before the sample. Up to five spectra were measured for each sample and averaged as to achieve statistics suitable for reliable quantitative XAFS data analysis.

The structural XAFS signals χ^{exp}, were extracted from the raw experimental data following the standards procedures for pre-edge subtraction and post-edge bare atomic background normalization [32] Quantitative XAFS data analysis has been performed along the lines already described [14] fitting the raw k-weighted XAFS spectra $k\chi^{exp}$ to the theoretical $k\chi^{th}$ curve (k is the photoelectron wavenumber, with m_e the electron mass, and E-Eo the photoelectron energy calculated as the difference between the x-ray energy E, and absorption edge energy Eo). The theoretical kχth model was calculated applying the standard XAFS formula [32]. The scattering amplitude, scattering phase and photoelectron mean free path functions were calculated using FEFF code [47] for atomic clusters generated on the basis of crystallographic structures. Partial contributions to the χ^{th} (neighbor shells) were assumed Gaussian shaped, the average neighbor distance (R_i), the multiplicity (coordination) number (N_i) and the mean square relative displacement (MSRD) (σ^2_i) parameters were obtained via least square data refinement using the FitEXA program [32]

UV-visible absorption measurements were performed on a Varian Cary 100 using quartz cells on solution in CH_2Cl_2 solvent.

UV-Visible emission measurements were performed on a Cary Eclipse Spectrophotometer. A Xenon arc lamp was used as excitation source. Both absorption and emission spectra were acquired on freshly prepared samples in CH_2Cl_2 solvent.

All measured optical properties and, in particular, the plasmon absorption, were stable in time and reproducible. This indicates that the capped nanoparticles are stable towards aggregation, i.e. the optical characterization results were not affected by aggregation.

Conclusions

The combined SR-XPS and XAS analysis carried out on AgNPs/**complex (1)** assemblies of different composition lead to investigate in detail the chemical structure and to correlate it with self-assembling behavior already observed by HR-TEM [8] and optical properties. Both XAFS and XPS data show that **complex (1)** molecules are intact upon linking AgNPs; on the other hand, **complex (1)** bonding to Ag atoms on NPs surface through S-Ag strong chemical bonds is observed in both S2p, Ag3d XPS and Ag, S -K-edge XAS data analysis, evidencing an Ag-rich AgS phase. Furthermore, both techniques individuate unusual behaviors of square-planar Pt(II) moieties, that can be explained by a rigid interaction between adjacent **complex (1)** chains (S-Pt-C contribution with low disorder in XAS; Pt4f electron acceptor in XPS). The obtained results, compared with the already published HR-TEM images, lead to figure out a complex structure of AgNPs/**complex (1)** hybrids, in which couples of silver NPs are linked through bridges made of assemblies **of complex (1)**. The observed S2p signal compatible with thiols physisorbed on metals or free thiols end groups, will belong to free **complex (1)** molecules or, more likely, to **complex (1)** molecules in the internal part of the self-assembled "bridge"; the more rigid Pt(II) square-planar moieties, will also belong to **complex (1)** molecules trapped in the middle of the self-assembled pattern, strongly interacting with the first neighbors.

The unique optical properties of these materials were also probed by UV-visible absorption and emission measurements and calculations. It was observed that, by varying the excitation wavelength in luminescence measurements, it is possible to finely tune both emission wavelengths and intensities; furthermore, excitation and emission wavelength corresponding to maximum emission intensity depend on NPs size. TDDFT calculations on a model system allowed to interpret the optical behavior of these nanomaterials. The calculated absorption profile is in excellent agreement with the experimental one. It has been possible to assign the two main features that can be seen: the band at low energy (425 nm) is due to the excitation of electrons from the HOMO (π) to the LUMO (σ*), and involve a charge transfer from the organometallic system to Ag center; the other band at higher energy (373 nm) is due to a π-π* absorption on the organometallic linker. This is consistent with the interpretation given above of the measured absorption profile where the low energy shoulder is precisely due to the metal nanoparticle. The emission profile can also be interpreted through the TDDFT results and our model suggests that the low energy emission band (430-500 nm) arises from the plasmon resonance excited states whereas the high energy one (350 nm) is due to organometallic linker. The tunability of the emission feature upon the irradiation energy supports the interest raised by these innovative materials for the exploitation of micro-nano sized optical devices.

Acknowledgements

The authors acknowledge for financial support Ateneo Sapienza 2011/C26A11PKS2 and 2013/C26A13HRZ4. This work has been partially supported by the Dipartimento di Chimica, Sapienza Università di Roma through the Supporting Reseach Initiative 2013.

Notes and references

[a] Roma Tre University, Department of Sciences and CISDiC, via della Vasca Navale 79 00146 – Rome (Italy).
[b] Sapienza University, Department of Chemistry, P.le A. Moro 5 00185 – Rome (Italy).
[c] IOM-CNR Laboratorio TASC, SS 14, Km 163,5 Basovizza, I-34149 – Trieste (Italy).
[d] Elettra-Sincrotrone Trieste S.C.p.A., S.S. 14 Km 163.5, 34149 Trieste, Italy

Electronic Supplementary Information (ESI) available: Table S1, Table S2, Table S3; Figure S1. See DOI: 10.1039/b000000x/

1 P. Zhao, N. Li, D. Astruc, *Coordination Chemistry Reviews*, 2013, **257**, 638– 665;
2 H. Xu and K. Suslick. *Adv. Mater.*, 2010, **22**, 1078-1082;
3 P. Crespo, R, Litran, T.C. Rojas, M. Multigner, J.M. de la Fuente, J.C. Sanchez-Lopez, M.A. Garcia, A. Hernando, S. Penades, A. Fernandez, *Phys. Rev. Lett.,* 2004, **93**, 087204 874;
4 Y. Yamamoto, T. Miura, M. Suzuki, M. Kawamura, H. Miyagawa, T. Nakamura, K. Kobayashi, T. Teranishi, H. Hori, *Phys. Rev. Lett.,* 2004, **93**, 116801 164;
5 M. Ranjan, S. Fackso, M. Fritzsche, S. Mukherjee, *Microelectronic Engineering,* 2013, **102**, 44-47;
6 R. Matassa, M. Carbone, I. Fratoddi, R. Caminiti, Journal of *Physical Chemistry B* 2010, **114**(7), 2359-2364;
7 I. Fratoddi, I. Venditti, C. Battocchio, G. Polzonetti, F. Bondino, M. Malvestuto, E. Piscopiello, L. Tapfer, M. V. Russo*, J. Phys. Chem. C*, 2011, **115**, 15198-15204;
8 R. Matassa, I. Fratoddi, M. Rossi, C. Battocchio, R. Caminiti, M. V. Russo, *J. Phys. Chem. C,* 2012, **116**, 15795−15800;
9 M. Quintiliani, M. Bassetti, C. Pasquini, C. Battocchio, M. Rossi, F. Mura, R. Matassa, L. Fontana, M.V. Russo, I. Fratoddi, *J Mater Chem C* 2014 in press, DOI:10.1039/C3TC32567A.
10 R. Vitaliano, I. Fratoddi, I. Venditti, G. Roviello, C. Battocchio, G. Polzonetti, M. V. Russo, J. Phys. Chem. A, 2009, **113** (52), 14730–14740J;
11 F. Vitale, R. Vitaliano, C. Battocchio, I. Fratoddi, C. Giannini, E. Piscopiello, A. Guagliardi, A. Cervellino, G. Polzonetti, M.V. Russo, L. Tapfer, *Nanosc. Res. Lett*., 2008, **3**, 461-467;
12 F. Vitale, R. Vitaliano, C. Battocchio, I. Fratoddi, E. Piscopiello, L. Tapfer, M.V. Russo, *J. Organomet. Chem*., 2008, **693**, 1043-1048;
13 G. Bunker Introduction to XAFS, Cambridge University Press 2010, ISBN-13 978-0-511-77001-2;
14 C. Battocchio, C. Meneghini, I. Fratoddi, I. Venditti, M. V. Russo, G. Aquilanti, C. Maurizio, F. Bondino, R. Matassa, M. Rossi, S. Mobilio, G. Polzonetti J. Phys. Chem. C, 2012, **116** (36), 19571–19578;
15 W-Y. Wong, P.D. Harwey, *Macromol. Rapid Commun.,* 2010, **31**, 671-713;
16 I. Fratoddi, G. Marghella, I. Venditti, D. Ferro, M.V. Russo, *J. Appl. Polym. Sci.* 2013, **128**, 304-309;
17 I. Fratoddi, E.S. Bronze-Uhle, A. Batagin-Neto, D.M. Fernandes, E. Bodo, C. Battocchio, I. Venditti, F. Decker, M.V. Russo, G. Polzonetti, C.F.O. Graeff, *J. Phys. Chem. A*, 2012*,* **116**, 8768−8774;
18 K. Nischala, T.N. Rao, N. Hebalkar, *Colloids Surf. B: Biointerfaces,* 2011, **82**, 203-208;
19 F. Vitale, R. Vitaliano, C. Battocchio, I. Fratoddi, E. Piscopiello, L. Tapfer, M.V. Russo, *J. Organomet. Chem*., 2008, **693**, 1043-1048;
20 M. Rycenga, C.M. Cobley, J. Zeng, W. Li, C.H. Moran, Q. Zhang, D. Qin, Y. Xia, *Chem. Rev.*, 2011, **111**, 3669-3712;
21 B. Gjonaj, J. Aulbach, P.M. Johnson, A.P. Mosk, L. Kuipers, A. Lagendijk, *Nature Photonics*, 2011, **5**, 360–363;
22 T. J. Hoheisel, J. Cordeiro, O. Lecarme, A. Cuche, C. Girard, E. Dujardin, D. Peyrade, A. Arbouet, *J. Phys. Chem. C,* 2013, **117**, 23126−23132
23 A. Sanchot, G. Baffou, R. Marty, A. Arbouet, R. Quidant, C. Girard, E. Dujardin, *ACS Nano,* 2012, **6**, 3434−3440;
24 S. J. Barrow, X. Wei, J. S. Baldauf, A. M. Funston, P. Mulvaney, *Nature*, 2012, **3**, 1275−1279;
25 M. A. Noginov, G. Zhu, A.M. Belgrave, R. Bakker, V. M. Shalaev, E. E. Narimanov, S. Stout, E. Herz, T. Suteewong, U. Wiesner, *Nature,* 2009, **460**, 1110-1112;
26 M. Brust, M. Walker, D. Bethell, D.J. Schiffrin, R. Whyman, *Chem. Commun.*, 1994, 801-802;
27 F. Vitale, L. Mirenghi, E. Piscopiello, G. Pellegrini, E. Trave, G. Mattei, I. Fratoddi, M.V. Russo, L. Tapfer, P. Mazzoldi, *Mat. Sci. Engin. C*, 2007, **27**, 1300–1304;
28 C.K. Yee, R. Jordan, A. Ulman, H. White, A. King, M. Rafailovich, J. Sokolov, *Langmuir*, 1999, **15**, 3486;
29 J.M. Tour, L. Jones, D.L. Pearson, J.J.S. Lamba, T.P. Burgin, G.M. Whitesides, D.L. Allara, A.N. Parikh, S.V. Atre, *J. Am. Chem. Soc.,* 1995, **117**, 9529-9534;
30 Y.D. Yu, R. Guan, H. Hashimoto, Y. Makita, *Acta Crystallographica B,* 1995, **51**, 149-155;
31 J. Löffler, J. Weissmüller, *Phys. Rev. B* 1995, **52**, 7076−7093;
32 C. Meneghini, F. Bardelli, S. Mobilio, *Nuclear Instrum. and meth. B,* 2012, **285**, 153-157;

33 C. Battocchio, F. D'Acapito, G. Smolentsev, A.V. Soldatov, I. Fratoddi, G. Contini, I. Davoli, G. Polzonetti, S. Mobilio, *Chemical Physics* 2006, **325**, 422–428;
34 I. Fratoddi, A. La Groia, C. Battocchio, M. V. Russo, *Journal of Polymer Science Part A: Polymer Chemistry*, 2007, **45** (15), 3311-3329
35 I. Fratoddi, C. Battocchio, A. Furlani, P. Mataloni, G. Polzonetti, M.V. Russo, *J. Organomet. Chem.*, 2003, **674**, (1–2), 10-23;
36 C. Battocchio, I. Fratoddi, M.V. Russo, V. Carravetta, S. Monti, G. Iucci, F. Borgatti, G. Polzonetti *Surface Science,* 2007, **601**, 3943–3947;
37 I. Fratoddi, C. Gohlke, C. Cametti, M. Diociaiuti, M.V. Russo, *Polymer,* 2008, **49**(15), 3211-3216;
38 S. Zhang, G. Leem, T.R. Lee, *Langmuir,* 2009, ***25***, 13855 3813860;
39 E. M. Goldys, M. A. Sobhan. *Advanced Functional Materials*, 2012, **22**, 1906 - 1913;
40 S. K. Ghosh, T. Pal, *Chem. Rev.* 2007, **107**, 4797−4862;
41 A. Batagin-Neto, E. S. Bronze-Uhle, D. M. Fernandes, I. Fratoddi, I. Venditti, F. Decker, E. Bodo, M. V. Russo, C. F. O. Graeff, *J. Phys. Chem. B*, 2011, **115**, 8047-8053;
42 D. D. Evanoff Jr., G. Chumanov, *Chem. Phys. Chem.*, 2005, **6**, 1221 - 1231;
43 Gaussian 09, Revision **D.01**, M. J. Frisch, G. W. Trucks, H. B. Schlegel, G. E. Scuseria, M. A. Robb, J. R. Cheeseman, G. Scalmani, V. Barone, B. Mennucci, G. A. Petersson, H. Nakatsuji, M. Caricato, X. Li, H. P. Hratchian, A. F. Izmaylov, J. Bloino, G. Zheng, J. L. Sonnenberg, M. Hada, M. Ehara, K. Toyota, R. Fukuda, J. Hasegawa, M. Ishida, T. Nakajima, Y. Honda, O. Kitao, H. Nakai, T. Vreven, J. A. Montgomery, Jr., J. E. Peralta, F. Ogliaro, M. Bearpark, J. J. Heyd, E. Brothers, K. N. Kudin, V. N. Staroverov, R. Kobayashi, J. Normand, K. Raghavachari, A. Rendell, J. C. Burant, S. S. Iyengar, J. Tomasi, M. Cossi, N. Rega, J. M. Millam, M. Klene, J. E. Knox, J. B. Cross, V. Bakken, C. Adamo, J. Jaramillo, R. Gomperts, R. E. Stratmann, O. Yazyev, A. J. Austin, R. Cammi, C. Pomelli, J. W. Ochterski, R. L. Martin, K. Morokuma, V. G. Zakrzewski, G. A. Voth, P. Salvador, J. J. Dannenberg, S. Dapprich, A. D. Daniels, nieFarkas, J. B. Foresman, J. V. Ortiz, J. Cioslowski, and D. J. Fox, Gaussian, Inc., Wallingford CT, 2009;
44 G. B. Kauffman, L. A. Teter, *Inorg. Synth*., 1963, **7**, 248-252;
45 S. Takahashi, Y. Kuroyama, K. Sonogashira, N. Hagihara, *Synthesis,* 1980, 627-630;
46 S. Pascarelli, F. Boscherini, F. D'Acapito, J. Hrdy, C. Meneghini, S. Mobilio, *J. Sinchrotron Rad.,* 1996, **3**, 147-155;
47 A.L. Ankudinov, B. Ravel, J.J. Rehr, S.D. Conradson, *Phys. Rev. B*, 1998, **58**, 7565.